Defect structures on epitaxial $Fe_3O_4(111)$ films

Sh. K. Shaikhutdinov,* M. Ritter, X.-G. Wang, H. Over, and W. Weiss†
Fritz-Haber-Institut der Max-Planck-Gesellschaft, Faradayweg 4-6, 14195 Berlin, Germany
(Received 26 May 1999)

Epitaxial $Fe_3O_4(111)$ films were grown onto a Pt(111) substrate by repeated cycles of iron deposition and subsequent oxidation in 10^{-6} mbar oxygen. A previous low energy electron diffraction (LEED) intensity analysis revealed the regular $Fe_3O_4(111)$ surface to expose $\frac{1}{4}$ monolayer Fe atoms over a close-packed oxygen layer underneath. With scanning tunneling microscopy (STM) a hexagonal lattice of protrusions with a 6 Å periodicity is observed. The protrusions are assigned to the topmost layer Fe atoms, which agrees with the dominating Fe3*d* electron density of states near the Fermi level related to these surface atoms, as revealed by *ab initio* spin-density-functional theory calculations. The most abundant type of point defects observed by STM are attributed to iron vacancies in the topmost layer, which was confirmed by LEED intensity calculations where different types of vacancy defects have been simulated. For oxidation temperatures around 870 K the regular $Fe_3O_4(111)$ surface coexists with several different surface structures covering about 5% of the films, which expose $\frac{3}{4}$ ML iron atoms or close-packed iron and oxygen layers, resulting in surface domains that are FeO(111) and $Fe_3O_4(111)$ in nature. These domains are arranged periodically on the surface and form ordered biphase superstructures. At 1000 K oxidation temperature they vanish and only the regular $Fe_3O_4(111)$ surface remains. [S0163-1829(99)07539-6]

I. INTRODUCTION

The relevance of metal oxides for technological applications like heterogeneous catalysis and others is prompting growing interest in investigating these materials. In this context, the preparation of thin epitaxial oxide films has become very important. They can be investigated by standard surface science techniques without facing a number of experimental problems encountered with single-crystal samples.[1] Regarding the catalytic properties of metal oxides, thin oxide films with defined surface structures and chemical compositions allow to investigate structure-reactivity correlations in a systematic manner.[2] However, the preparation of defined oxide surfaces is difficult and critically depends on preparation parameters like oxidation temperature and oxygen partial pressure.[3] A recent systematic investigation revealed Fe- and O-terminated surface structures to coexist on epitaxial α-$Fe_2O_3(0001)$ films prepared in a wide range of oxygen gas pressures,[4] until at 1 mbar oxygen pressure the O-terminated surface dominates as predicted by recent *ab initio* calculations.[5] Thus, the formation and possible coexistence of different surface structures always has to be taken into account. Furthermore, atomic surface defects can dominate the catalytic properties rather than the well-ordered surface areas, as was shown for example for the dehydrogenation of ethylbenzene to styrene over Fe-terminated α-$Fe_2O_3(0001)$ model catalyst surfaces.[6] Therefore, the identification and characterization of surface defects is crucial in order to comprehend the catalytic properties of metal-oxide surfaces. With scanning tunneling microscopy (STM) it is possible to image coexisting surface structures as well as local defects. However, the assignment of image contrasts to atomic species needs additional information, in particular for compound materials like metal oxides, which contain several elemental species. Such additional information can be provided for instance by low energy electron diffraction (LEED) and *ab initio* calculations.

Previous STM studies performed on natural $Fe_3O_4(111)$ single-crystal samples prepared in 10^{-6} mbar oxygen revealed the coexistence of two different surface terminations.[7] One was attributed to an unreconstructed (111) termination of Fe_3O_4 that exposes $\frac{1}{4}$ monolayer (ML) of O atoms over $\frac{3}{4}$ ML of Fe atoms, the other to an unreconstructed (111) termination that exposes $\frac{1}{2}$ ML of iron atoms over a close-packed oxygen layer. On surfaces prepared under more reducing conditions, i.e., brief annealing in high vacuum without oxygen, coexisting FeO(111) and $Fe_3O_4(111)$ surface domains formed ordered superstructures.[8] This phenomenon was called biphase ordering, which for the first time was observed on α-$Fe_2O_3(0001)$ single-crystal surfaces prepared in 10^{-6} mbar oxygen. Here, FeO(111) and α-$Fe_2O_3(0001)$ patches formed long-range superstructures as a result of the reducing preparation conditions for the Fe_2O_3 oxide phase.[9]

In this paper, we focus on surface defect structures that form on well-ordered epitaxial $Fe_3O_4(111)$ films grown onto Pt(111) substrates. One single regular surface structure is observed after oxidation at 1000 K in 10^{-6} mbar oxygen, whose atomic geometry was determined in a LEED intensity analysis.[10] Based on the LEED analysis result and on *ab initio* calculations the protrusions observed in atomic resolution STM images of this surface can be assigned to topmost layer Fe atoms, as discussed in Sec. III A. The dominant type of point defect observed by STM appears as missing protrusion and is assigned to surface Fe vacancies, which also is confirmed by dynamical LEED calculations. In Sec. III B STM images of ordered biphase structures that consist of $Fe_3O_4(111)$ and FeO(111) surface domains are presented. They form at oxidation temperatures around 870 K and represent minority defect structures that cover about 5% of the entire sample. Based on the STM data models for these

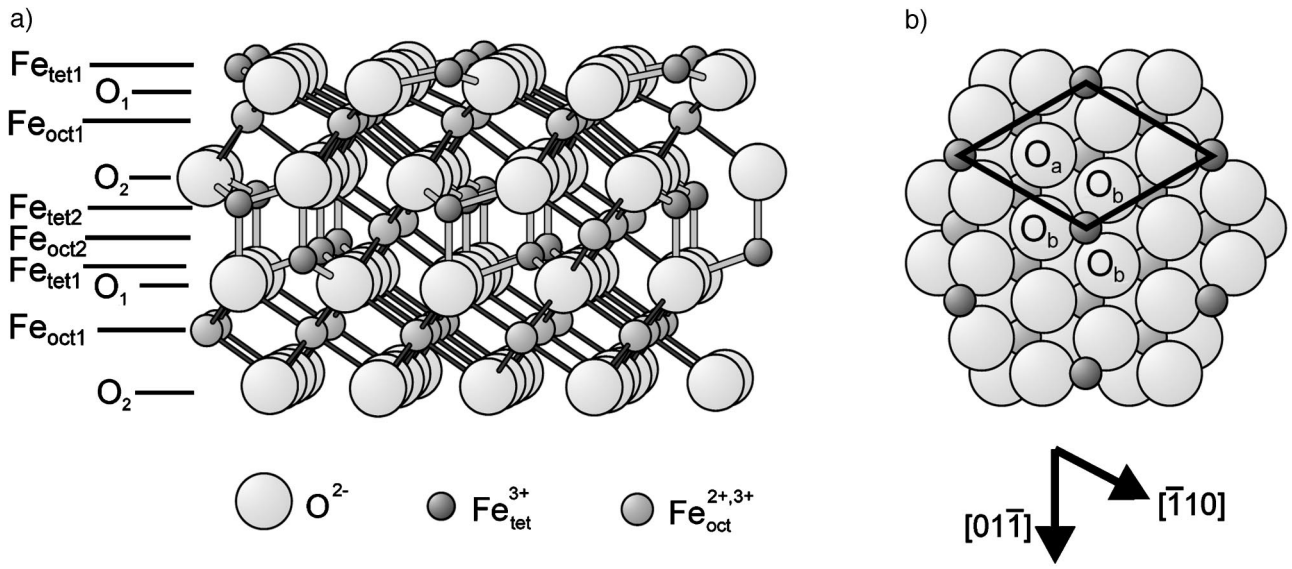

FIG. 1. Slightly tilted side view (a) and top view (b) of the $Fe_3O_4(111)$ surface structure as determined by the LEED intensity analysis. On the left side the (111) layer sequence with tetrahedrally coordinated Fe_{tet1} or Fe_{tet2} atoms, with octahedrally coordinated Fe_{oct1} or Fe_{oct2} atoms, and with O_1 and O_2 layers is indicated. In (b) the surface unit cell with a lattice constant of 5.94 Å and the two symmetrically inequivalent oxygen atoms O_a and O_b are indicated. In the side view the ionic radii are reduced by a factor of 0.5, the top view is drawn with the full ionic sizes.

structures are proposed, and a comparison to similar biphase structures observed on $Fe_3O_4(111)$ single crystal samples is made.

II. EXPERIMENT

The experiments were performed in an ultrahigh vacuum (UHV) system described in detail elsewhere.[11] It had a base pressure of less than 1×10^{-10} mbar and was equiped with a STM, a backview LEED optics, an Auger electron spectrometer (AES), and standard facilities for sample cleaning. The Pt(111) surface was cleaned by repeated cycles of argon sputtering and annealing to 1300 K, until it exhibited a sharp (1×1) LEED pattern and no contamination signals in the Auger electron spectra. The preparation and growth of the epitaxial $Fe_3O_4(111)$ films is described in detail in Ref. 12. Briefly, iron was deposited by an electron beam-assisted evaporator onto the platinum substrate kept close to room temperature, followed by oxidation for two minutes in 10^{-6} mbar oxygen at 1000 K. This produces a well-ordered FeO(111) monolayer film, which can be identified by its characteristic LEED pattern.[12] The oxygen in the UHV chamber is pumped off after the sample temperature falls below about 700 K. When the first FeO(111) monolayer has formed the oxidation temperature was decreased to 870 K, and after numerous deposition-oxidation cycles $Fe_3O_4(111)$ multilayer films at least 100 Å thick were obtained. These films exhibited LEED patterns with sharp spots and no AES contamination signals. Final annealing treatments were performed for 5 min in 10^{-6} mbar oxygen at 870–1000 K.

The STM measurements were made at room temperature in the constant-current mode. Tungsten tips were etched electrochemically in three-molar NaOH solution and cleaned by electron bombardment under UHV conditions. Image processing of the experimental data included background subtraction and smoothing procedures. LEED intensity-voltage (I-V) curves were measured under normal incidence at $T\approx120$ K sample temperature. The diffraction patterns were recorded with a charge coupled device camera and stored onto a computer, then the I-V curves were extracted with software programs developed at the Fritz-Haber Institut.

III. RESULTS AND DISCUSSION

Fe_3O_4 magnetite crystallizes in the cubic inverse spinel structure, where the oxygen anions form a close-packed fcc sublattice with tetrahedrally and octahedrally coordinated Fe^{2+} and Fe^{3+} cations located in the interstitial sites.[13] Figure 1 depicts side and top views of the $Fe_3O_4(111)$ surface structure determined by the LEED intensity analysis.[10] The hexagonal close-packed oxygen (111) layers form a cubic *ABCABC*... stacking sequence along the [111] direction, the interatomic distance within these planes is 2.96 Å. Two different oxygen atom positions exist with respect to the $p3m1$ symmetry of the $Fe_3O_4(111)$ surface, which are labeled O_a and O_b in the top view of Fig. 1(b). Between the oxygen planes (111) planes tetrahedrally and octahedrally coordinated Fe atoms are located. Since not all possible sites are occupied within these Fe(111) planes, two-dimensional hexagonal unit cells with a lattice constant of 5.92 Å are formed. Six ideal bulk terminations can be obtained by cutting the spinel (111) stacking sequence, which are indicated by the letters on the left side of Fig. 1(a). Defining the atom density of a close-packed oxygen layer as 1 ML, these terminations can expose $\frac{1}{4}$ ML of tetrahedrally coordinated Fe_{tet1} or Fe_{tet2} atoms, $\frac{3}{4}$ ML of octahedrally coordinated Fe_{oct1} or Fe_{oct2} atoms, or close packed O_1 or O_2 layers. The distance between two equivalent $Fe_3O_4(111)$ terminations is 4.85 Å.

A. Regular $Fe_3O_4(111)$ surface structure

The dynamical LEED intensity analysis revealed the regular $Fe_3O_4(111)$ surface to form an unreconstructed bulk

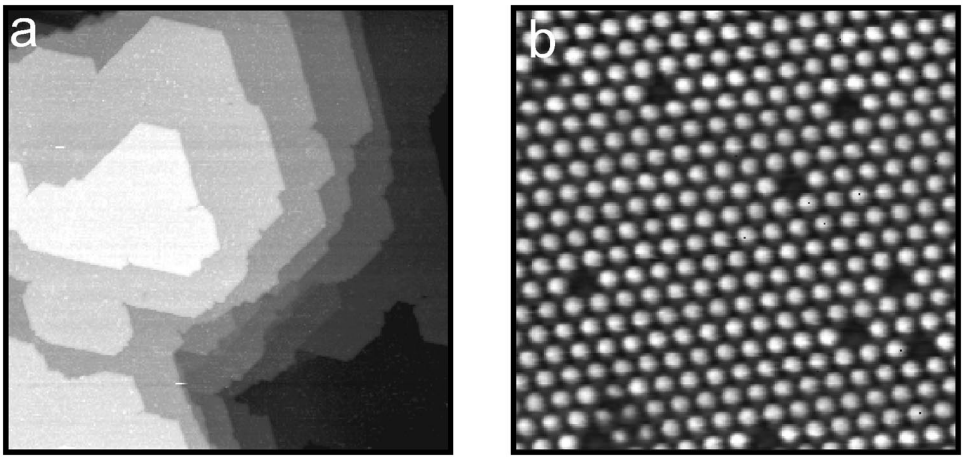

FIG. 2. (a) $3000\times3000\,\text{Å}^2$ STM image showing the characteristic morphology of the $Fe_3O_4(111)$ films. Atomically flat terraces up to 1000 Å wide are separated by atomic steps ~5 Å high. $U_t=1.4\,\text{V}$, $I_t=0.8\,\text{nA}$. (b) $90\times90\,\text{Å}^2$ STM image of the regular $Fe_3O_4(111)$ surface. Protrusions form a hexagonal lattice with a 6 Å periodicity. They are attributed to the topmost layer Fe_{tet1} atoms [see Fig. 1(b)], the missing protrusions to Fe_{tet1} vacancies. $U_t=-0.9\,\text{V}$, $J_t=0.5\,\text{nA}$.

termination that exposes $\frac{1}{4}$ ML of Fe_{tet1} atoms over a close-packed oxygen layer underneath. It can be described by the layer sequence $Fe_{tet1}-O_1-Fe_{oct1}-O_2-Fe_{tet2}-Fe_{oct2}-\cdots$. Numerical comparison of the I-V curves calculated for the best-fit structure depicted in Fig. 1 and I-V curves taken from an $Fe_3O_4(111)$ film with a low-surface defect concentration results in a Pendry-*R* factor of 0.20 for a total energy range of 1300 eV. Strong relaxations of the upper four interlayer distances were found. The first two interlayer distances are contracted by 41 and 26%, the third one is expanded by 15% and the forth one is contracted by 11%. These relaxations stabilize the polar $Fe_3O_4(111)$ termination by considerably changing the electron density of states at the surface.[10] This regular structure is formed on the entire surface of films prepared by oxidation at $T=1000\,\text{K}$, several additional minority structures coexist for oxidation temperatures around 870 K as will be discussed in Sec. III B. On all films we observe the same hexagonal LEED pattern (not shown here). It corresponds to a surface unit cell with a lattice constant of ≈6 Å, which is formed by the topmost Fe_{tet1} atoms as depicted in Fig. 1(b).

Figure 2(a) shows a $3000\times3000\,\text{Å}$ STM image that depicts the characteristic film morphology. Atomically flat terraces up to 1000 Å in size can be seen, which are separated by steps oriented along the main crystallographic directions on the (111) plane. All steps are 4.8 Å high, which corresponds to the distance between equivalent $Fe_3O_4(111)$ surface terminations. On a length scale of 1 μm the vertical roughness ranges around 50 Å and mainly depends on the substrate morphology. Some screw dislocations are observed on the films (not shown here). Figure 2(b) shows a $90\times90\,\text{Å}$ atomic resolution STM image of the regular $Fe_3O_4(111)$ surface. A hexagonal lattice of protrusions with a 6 Å periodicity and a corrugation amplitude of about 1 Å can be seen, as well as randomly distributed point defects that appear as missing protrusions. They represent the dominant type of surface point defects we observed on all films, and their concentration varies from film to film. The same characteristic hexagonal lattice of protrusions with randomly distributed vacancy defects is observed for both positive and negative tunneling bias voltages with magnitudes between 0.3 and 1.5 V, without significant changes in the image contrast.

An assignment of the atomic features in these STM images to surface atoms needs additional information. The $Fe_3O_4(111)$ surface structure determined by the LEED analysis depicted in Fig. 1 strongly suggests that the STM protrusions correspond to the positions of the Fe_{tet1} cations in the topmost layer, since they form the same hexagonal surface lattice with a 6 Å periodicity. This interpretation is further substantiated by *ab initio* spin-density-functional theory calculations performed for this particular surface termination of Fe_3O_4.[5] These calculations revealed interlayer relaxations along the same directions as obtained from the LEED analysis, which will be published elsewhere. The electron density of states (DOS) at the surface was calculated for the relaxed $Fe_3O_4(111)$ surface structure determined by the LEED analysis, which was found not to depend strongly on the absolute values of the interlayer relaxations. Figure 3 depicts the atom projected partial DOS of the first two atom layers. It can be seen that the dominant contribution is related to Fe3*d* orbitals of the topmost Fe_{tet1} atoms, which create two sharp DOS maxima located just above and below the Fermi level. Therefore, this result also indicates that the STM protrusions correspond to the Fe_{tet1} atom positions, and it explains the bias independence of the STM images. The surface DOS considerably differs from the one in bulk Fe_3O_4, as observed for many metal oxides.[14] The ionic bond character decreases and the bonds become more covalent at the surface,[15,16] which stabilizes the polar $Fe_3O_4(111)$ surface termination as discussed in Ref. 10.

The assignment of the STM protrusions to topmost layer Fe_{tet1} atoms suggests the dominating type of point defect, which is imaged as a missing protrusion, to correspond to a missing Fe_{tet1} atom on the surface. Missing surface atoms can be approximated in LEED intensity calculations with the averaged *t*-matrix approach (ATA).[17] The introduction of a term $c\cdot t$ (c = concentration of the atomic species, $0\leqslant c\leqslant1$; t = atomic scattering matrix) allows to simulate variable concentrations of any atomic species randomly distributed on

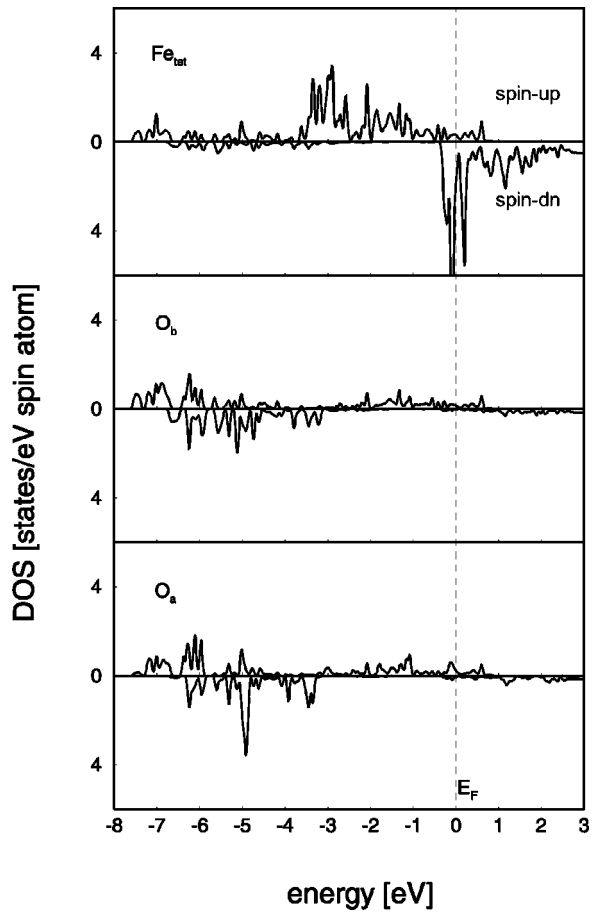

FIG. 3. Atom projected partial electron density of states for the first two atom layers of the $Fe_3O_4(111)$ surface termination depicted in Fig. 1, obtained from *ab initio* spin-density-functional theory calculations. Near the Fermi level E_F the DOS is dominated by $3d$ states related to Fe_{tet1} surface atoms, $2p$ states related to the two symmetrically inequivalent O_a and O_b atoms dominate at binding energies below -4 eV.

the surface lattice sites. As mentioned above these defects occur in varying concentrations on different films, which offers the possibility to identify them via a LEED intensity analysis of a high-defect-density data set. Figure 4 shows two experimental I-V curve data sets taken from films with high- and low-surface defect concentrations, as deduced from STM measurements prior to the data aquisition. From a visual inspection these I-V curves look quite different. A quantitative comparison between the two experimental data sets reveals a Pendry-*R* factor of $R_P = 0.19$, which indicates some significant differences in the corresponding surface structures. However, both data sets lead to identical best fit structures for the $Fe_3O_4(111)$ surface (within the margins of error) when performing a structure analysis with the two experimental LEED I-V data sets, where the low-defect density data set reveals a lower *R* factor than the high-defect-density data set. Therefore, we assign the differences in the I-V curves to the different defect concentrations of the two film surfaces, as observed by STM.

For simulating the two LEED I-V data sets in Fig. 4 we tested different types of surface vacancies and varied their concentrations from 0% up to 50% in steps of 10%. Removal of O_a atoms (cf. model in Fig. 1) always increased R_P for the

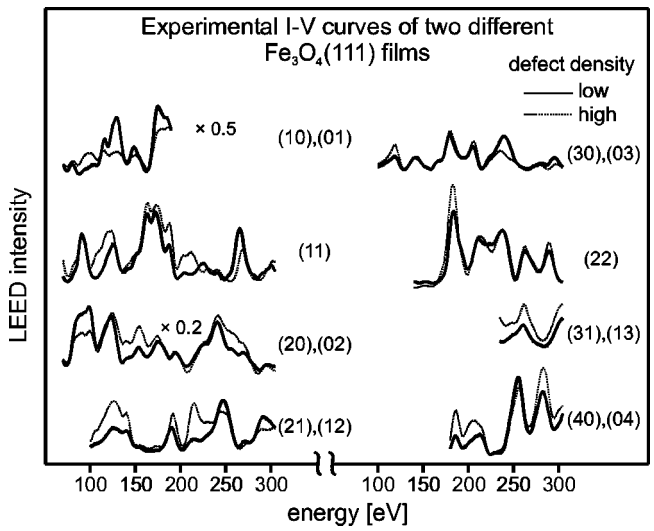

FIG. 4. Comparison of experimental IV curves taken from $Fe_3O_4(111)$ films with a high-surface defect density (dashed lines) and with a low-surface defect density (solid lines). The agreement of the two experimental data sets is quantified by an overall Pendry-*R* factor of 0.19.

high-defect-density data set. Only a negligible improvement of the Pendry-*R* factor was achieved after removing a topmost layer Fe_{tet1} atom together with the three O_b atoms underneath. In contrast, R_P decreased upon removing the topmost Fe_{tet1} atoms. The maximal improvement of R_P was 15% for a defect concentration of 30%. No improvement of R_P for the low-defect-density data set was achieved when considering these defects in the LEED intensity calculations. Altogether, the simulation of defects as missing Fe_{tet1} atoms improved the fit with the high-defect-density data set, while the introduction of oxygen vacancies increased the Pendry-*R* factor. This result further corroborates the assignment of the protrusions in the STM images to the positions of topmost layer Fe_{tet1} atoms and the dominating type of surface point defect to Fe_{tet1} vacancies.

B. Biphase structures on $Fe_3O_4(111)$

A number of structures with short-range periodicities of 3 and 6 Å were formed after preparation at lower temperatures of 870 K. They differ from the regular $Fe_3O_4(111)$ surface structure and are arranged in patches that form long-range superstructures as shown in Fig. 5(a) These superstructure islands have lateral sizes of 100–500 Å, they are randomly distributed on the surface and cover less than 5% thereof. Three characteristic structural arrangements are observed within these regions.

Structure 1

The lower part of Fig. 5(b) shows the regular $Fe_3O_4(111)$ surface exhibiting the hexagonal lattice of protrusions with a 6 Å periodicity. In the upper part a long-range superstructure is formed by three distinct regions labeled α, β, and γ. The hexagonal superstructure cell has a lattice constant of 45 Å and is aligned to the $Fe_3O_4(111)$ surface unit cell. The protrusions within the α regions are 6 Å apart from each other

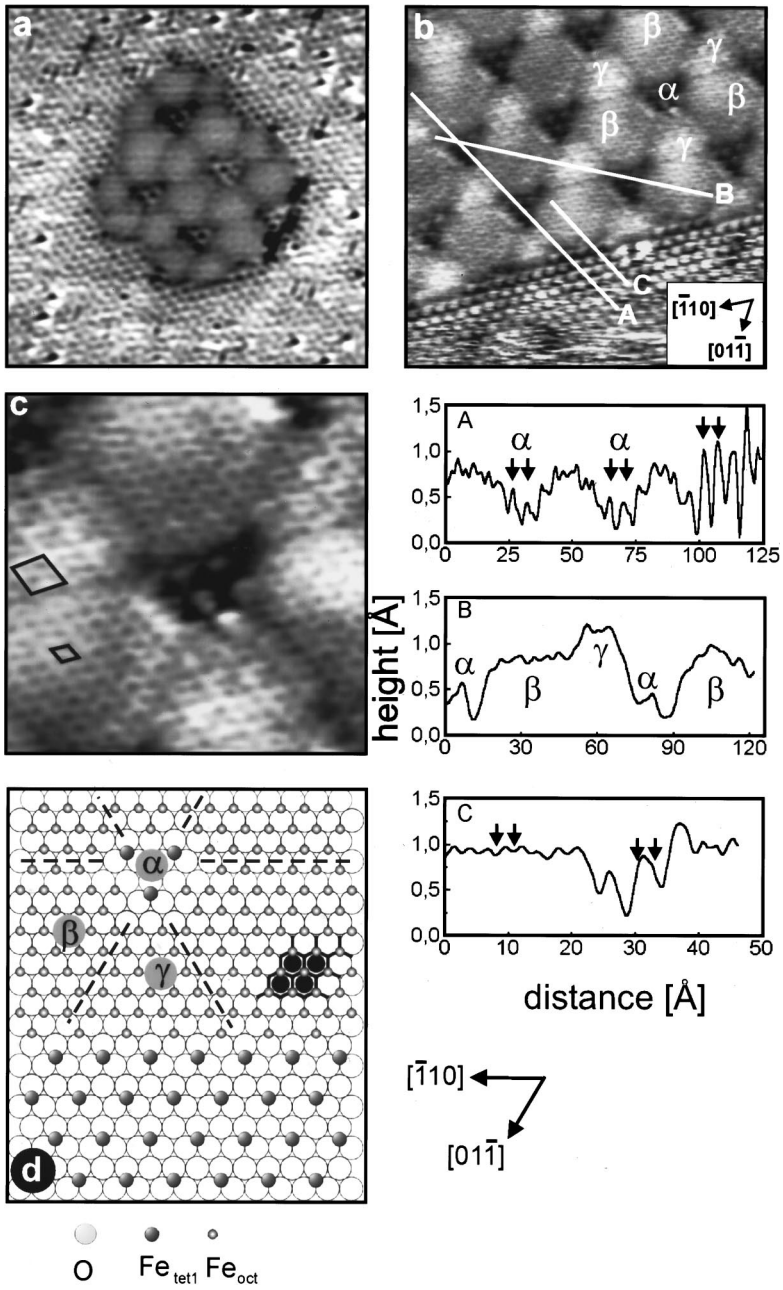

FIG. 5. STM images of an $Fe_3O_4(111)$ film prepared at 870 K in 10^{-6} mbar oxygen. (a) 200×200 Å^2 image showing an island exhibiting a superstructure involving three different surface structures, which is surrounded by the regular $Fe_3O_4(111)$ surface. $U_t=0.7$ V, $I_t=0.5$ nA. (b) 140×140 Å^2 image of a superstructure region. Three distinct regions labeled α, β, and γ form a superstructure with a ~45 Å periodocity and aligned to the regular $Fe_3O_4(111)$ surface lattice visible in the lower part of the image. $U_t=0.65$ V, $I_t=1.2$ nA. Below profile lines along the white lines labeled *A*, *B*, and *C* in the STM image are shown. (c) 55×55 Å^2 image of a superstructure region. Hexagonal arranged protrusions form a 6 Å lattice in the α region. Hexagonal lattices of depressions with 3 Å periodicities can be seen in the β and γ regions. An additional corrugation modulation creates a 6 Å unit cell in the γ region. $U_t=0.6$ V, $I_t=0.5$ nA. (d) Schematic model for the surface structures formed in the α, β, and γ regions. In the lower part the regular $Fe_3O_4(111)$ surface terminated by $\frac{1}{4}$ ML Fe_{tet1} atoms is depicted, which is also formed in the α region. The β and γ regions expose hexagonal close-packed layers of octahedrally coordinated Fe atoms located over an O_1 layer, resulting in surface structures FeO(111) in nature. The dark circles on the right indicate the minimum electron density of states located over the O_1 atoms in the second layer, because the dangling bonds of the octahedrally coordinated Fe atoms are oriented ''tangential'' to the O_1 atoms.

and located in lateral registry with the protrusions of the surrounding regular $Fe_3O_4(111)$ surface. Therefore, we assign them to the same layer of Fe_{tet1} atoms, although the profile line *A* in Fig. 5 reveals the α region to be located ~0.6 Å deeper than the regular $Fe_3O_4(111)$ surface. This can also be seen in Fig. 5(a) where the entire superstructure island looks somewhat deepened into the surrounding $Fe_3O_4(111)$ surface, from which it is separated by a dark periphery about 10 Å wide. The apparent height difference presumably is caused by a different electron density of states on the superstructure surface region when compared to the surrounding regular $Fe_3O_4(111)$ surface.

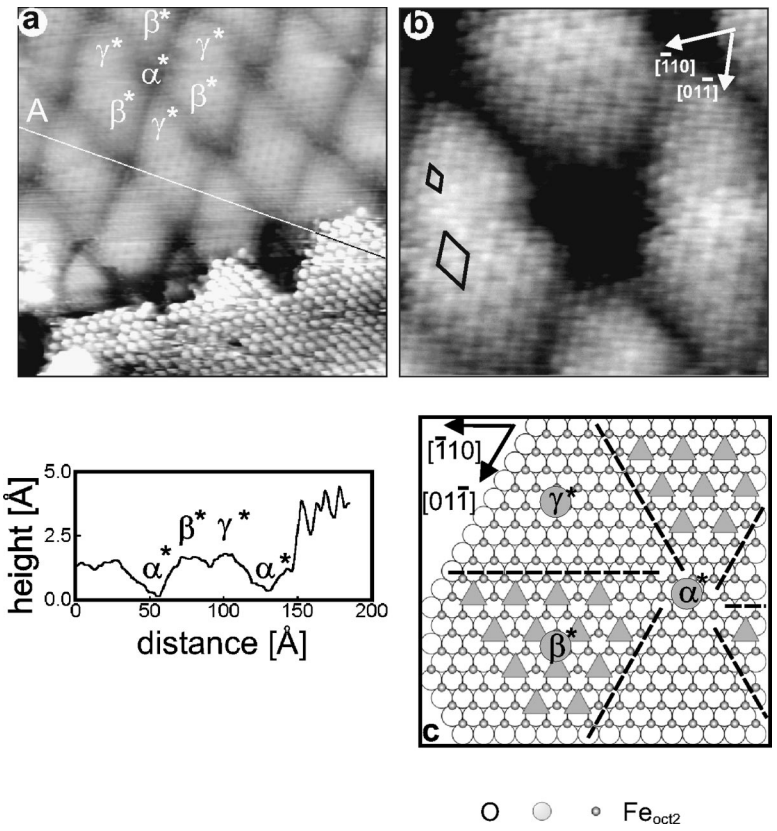

FIG. 6. (a) 175×175 Å^2 image showing a biphase superstructure and a profile line along the white line in the image (below). The biphase superstructures are located 2.5 Å lower than the regular $Fe_3O_4(111)$ surface visible in the lower part of the image, and they are slightly rotated against the regular $Fe_3O_4(111)$ surface lattice. Like in Fig. 4 three distinct regions α^*, β^*, and γ^* are indicated. $U_t=0.2$ V, $I_t=0.5$ nA. (b) 70×70 Å^2 image showing hexagonal lattices of protrusions with 3 Å periodicities in the β^* and γ^* regions, whereas no features are visible in the α^* region. In the β^* region $\frac{1}{4}$ ML of protrusions are missing, leading to a 6-Å surface unit cell. (d) Schematic models for the surface structures in the β^* and γ^* regions. The gray triangles in the β^* region indicate the depressions observed in (b). $\frac{3}{4}$ ML of Fe_{oct1} atoms are exposed over an O_2 layer underneath, resulting in an $Fe_3O_4(111)$ surface termination. In the γ^* region a close-packed Fe layer is exposed over an O_2 layer underneath, resulting in a $Fe_3O_4(111)$ surface terminated by a FeO(111) bilayer. $U_t=0.2$ V, $I_t=0.4$ nA.

For the interpretation of the STM features within the β and γ regions we refer to the Fe_{tet1} atom layer within the α regions. As can be seen in Fig. 5(c) the β and γ regions exhibit similar structures, imaged as depressions with a 3 Å periodicity and much smaller corrugation amplitudes than those observed in the α regions. The β and γ regions are separated by a narrow darker region in between, which cannot be assigned to an antiphase domain boundary since the depressions within both regions are in lateral registry. They form well ordered structures with a 3 Å unit cell in the β region, whereas a 6 Å unit cell is formed in the γ region because of an additional corrugation modulation. These unit cells are indicated in Fig. 5(c). In the profile lines *A* and *B* the corrugation maxima within the β and γ regions appear about 0.4 Å higher than the protrusions in the α region. Therefore, we assign them to a surface terminated by a hexagonal close-packed layer of Fe_{oct2} atoms located in threefold hollow sites on top of the O_1 layer. In a truncated bulk model without relaxations the Fe_{oct2*} layer would be located 0.6 Å higher than the Fe_{tet1} layer, which compares reasonably with the measured height difference of 0.4 Å. The stacking sequence of this termination can be described as $Fe_{oct2*}-O_1-Fe_{oct1}-O_2-Fe_{tet2}\ldots$, where the asteric indicates that the topmost Fe_{oct2*} layer contains 1-ML Fe atoms in contrast to $\frac{3}{4}$ ML in bulk Fe_3O_4. This termination corresponds to a surface structure FeO(111) in nature, where the O_1 plane is located between two octahedrally coordinated Fe layers.

Figure 5(d) schematically depicts the proposed model with the regular $Fe_3O_4(111)$ surface structure in the lower part and the three superstructure regions in the upper part. They all expose Fe atoms located over the same O_1 layer. Because of their octahedral coordination each Fe atom in the β and γ regions has three dangling bonds, which are oriented tangential to the oxygen atoms underneath in a top view. This produces a honeycomb lattice with a minimum electron density of states located in the hollow sites of the close-packed Fe lattice, that is on top of the oxygen atoms underneath. The minimum electron density of states is depicted schematically by the black circles in the right part of Fig. 5(d). Therefore, we assign the depressions in the STM images to oxygen atom positions in the O_1 layer. The pair of arrows on the left-hand side in the line profile *C* mark two depressions, the pair of arrows on the right-hand side were laterally shifted by an integer number of lattice spacings, until they were located over the α region. It can be seen that the protrusions attributed to Fe_{tet1} atoms are between two depressions located at oxygen atom positions, as expected for the model depicted in Fig. 5(d). The additional modulation in the γ region creating the 6 Å unit cell must be due to a somewhat different surface layer relaxation if compared to region β exhibiting the 3 Å unit cell.

Structure 2

The upper part of Fig. 6(a) depicts a similar superstructure as observed in Fig. 5. It forms a large unit cell with a lattice constant of 45 Å, which is slightly rotated against the regular $Fe_3O_4(111)$ surface lattice visible in the lower part of the image. Again, three distinct regions labeled α^*, β^*, and γ^* can be distinguished within each superstructure cell. Here, no protrusions are observed within the α^* regions. The β^* and γ^* regions exhibit hexagonal lattices of protrusions with a 3 Å periodicity, which are aligned to the regular $Fe_3O_4(111)$ surface lattice. In the β^* region missing protrusions create triangular shaped depressions forming a 6 Å unit cell as resolved in Fig. 6(b), whereas the γ^* region exhibits a

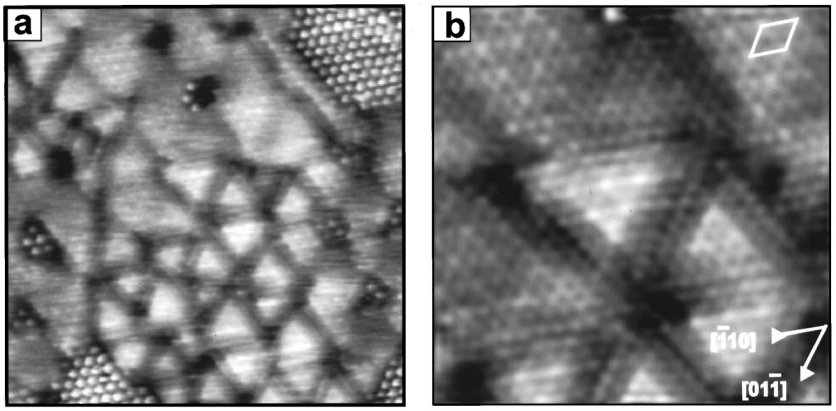

FIG. 7. (a) 200×200 Å^2 image showing a variety of long-range structures that do not form ordered superstructures. They are located on about the same level as the regular $Fe_3O_4(111)$ surface. $U_t=0.3$ V, $I_t=0.4$ nA. (b) 65×65 Å^2 image showing hexagonal lattices of protrusions with a 3 Å periodicity. The lateral positions of the protrusions are in registry with threefold hollow sites of the Fe_{tet1} atom positions on the regular $Fe_3O_4(111)$ surface. They are attributed the oxygen atom positions of a $Fe_3O_4(111)$ surface terminated by an O_1 layer. $U_t=0.3$ V, $I_t=0.4$ nA.

close-packed lattice of protrusions with a 3 Å periodicity. As can be seen in the profile line in Fig. 6 these two regions are located on the same height, which is about 2.5 Å lower than the regular $Fe_3O_4(111)$ regions. This height difference corresponds to the spacing between consecutive oxygen (111) layers within the Fe_3O_4 bulk structure. Therefore, we propose these regions to be terminated by Fe atoms located over an O_2 layer (see Fig. 1). As depicted schematically in Fig. 6(c), a close-packed layer of octahedrally coordinated Fe_{oct1} atoms is exposed in the γ^* region. This termination is described by the layer sequence $Fe_{oct1*}-O_2-Fe_{tet2}-Fe_{oct2}-Fe_{tet1}-O_1-\ldots$, which corresponds to an FeO(111) bilayer located on top of a $Fe_3O_4(111)$ surface terminated by a Fe_{tet2} layer. The β^* region is terminated by $\frac{3}{4}$ ML of Fe_{oct1} atoms, which create the hexagonal lattice of depressions with a 6-Å periodicity as indicated by the triangles in Fig. 5(c). This corresponds to an unreconstructed bulk termination of $Fe_3O_4(111)$.

Structure 3

Figure 7(a) shows a STM image where mostly triangular-shaped regions separated by narrow dark boundary lines can be seen. The regular $Fe_3O_4(111)$ surface is visible in upper right and lower left of the image. Here, the long-range modulations form no ordered superstructure. The high-resolution image in Fig. 7(b) exhibits a hexagonal lattice of protrusions with a 3 Å periodicity. They are located on about the same level as the regular $Fe_3O_4(111)$ surface, and therefore, we attribute them to be based on the O_1 layer. The protrusion amplitudes are modulated and form a unit cell with a lattice constant of 6 Å. Their lateral positions are in registry with threefold hollow sites of the Fe_{tet1} atom positions on the regular $Fe_3O_4(111)$ surface. This lateral position corresponds either to an O_a atom position or to a hollow site over three O_b atoms (see Fig. 1). Therefore, we attribute these protrusions to the topmost layer oxygen atoms of a $Fe_3O_4(111)$ surface terminated by an O_1 layer.

As outlined in the introduction similar biphase structures with FeO(111) surface domains were observed on natural α-$Fe_2O_3(0001)$ and $Fe_3O_4(111)$ single crystal samples.[8,9] On $Fe_3O_4(111)$ the same termination exposing $\frac{3}{4}$-ML Fe_{oct1} atoms over an O_2 layer was observed, and similar models were proposed for FeO(111) surface domains exposing close-packed iron or oxygen layers. In the single-crystal experiments the FeO(111) surface domains were formed because of the reducing preparation conditions for the respective oxide phases, caused by the low-oxygen partial pressures applied. Here, the biphase structures on the epitaxial $Fe_3O_4(111)$ films were formed in 10^{-6} mbar oxygen pressure at $T=870$ K. According to the iron-oxygen bulk phase diagram Fe_3O_4 magnetite is the thermodynamically stable phase under these conditions.[18] The FeO surface domains might be formed because of the slow kinetics of the oxidation of Fe to FeO and Fe_3O_4 during the preparation procedure. This explains why these regions disappear at higher oxidation temperatures of 1000 K, when only the regular $Fe_3O_4(111)$ surface remains which is the most stable structure. It is interesting to note that Thornton *et al.* have observed regions on the $Fe_3O_4(111)$ single crystals that looked identical to the STM images of the regular $Fe_3O_4(111)$ surface regions presented here.[8] These regions increased in size with increasing annealing temperature, which also suggests this structure to be the most stable one.

In the course of the experiments it turned out that the regular $Fe_3O_4(111)$ surface is very reactive towards adsorption. After some hours under UHV condition the bright features in Fig. 8 are observed. They create corrugation maxima about 2 Å high, which are located on threefold hollow sites (arrow 3) and on top sites (arrow 2) of the underlying hexagonal lattice of protrusions. The appearance of these adsorbate features strongly depends on the bias voltage. They are not visible at negative voltages and at positive voltages below 0.3 V, at higher positive voltages they become visible as bright protrusion features. These corrugation changes were reproducible when the bias voltage was changed during scanning, which excludes tip changes as a reason. The adsorbate coverage in Fig. 8 corresponds to about 3% of a ML, referred to the atom density in the close-packed oxygen (111) layers of Fe_3O_4. Since no elements other than Fe and O are detected with AES, these features must correspond to

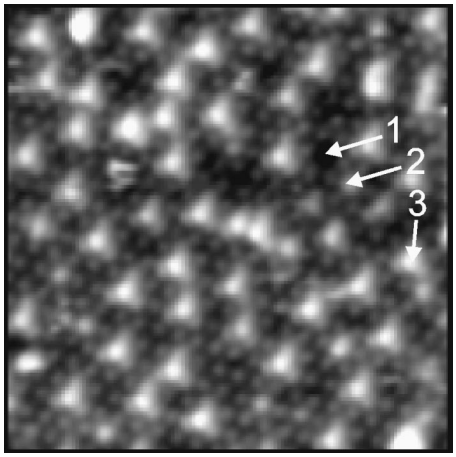

FIG. 8. 125×125 Å^2 image of the regular $Fe_3O_4(111)$ surface covered by adsorbate species, which appear as bright features under these tunneling conditions. $U_t=1.3$ V, $I_t=1.0$ nA. Arrow 1 marks a surface Fe_{tet1} vacany, arrow 2 and 3 adsorbate species on top and threefold hollow site, respectively.

adsorbed water, OH, or H species. We never observed adsorbate features on the biphase superstructure regions, which indicates a very different surface chemistry for these terminations. The nature of these adsorbate species is currently under investigation.

IV. SUMMARY

The atomic surface structures and defects formed on epitaxial $Fe_3O_4(111)$ films were investigated with STM and LEED. For oxidation temperatures of 1000 K one stable surface termination is formed. A previous LEED intensity analysis performed for this regular $Fe_3O_4(111)$ surface structure suggests the protrusions measured in atomic resolution STM images to correspond to the Fe atom positions in the topmost surface layer. This assignment agrees with the electron density of states obtained from *ab initio* spin-density-functional theory calculations performed for this surface termination, where Fe3*d* derived states of the surface Fe atoms dominate close above and below the Fermi level. The dominant type of surface point defects appear as a missing protrusion and therefore are attributed to iron vacancies in the surface layer, which was corroborated by simulation of various kinds of surface vacancy defects with dynamical LEED calculations.

For lower oxidation temperatures of 870 K domains with several additional surface structures are formed. They cover about 5% of the film surfaces and expose $\frac{3}{4}$-ML Fe atoms as well as close-packed iron and oxygen layers, which correspond to surface terminations that are $Fe_3O_4(111)$ and FeO(111) in nature, respectively. These domains are arranged periodically and form long-range superstructures, resulting in the biphase ordering phenomenom observed previously on $Fe_3O_4(111)$ single-crystal samples.

ACKNOWLEDGMENTS

We thank Robert Schlögl and Matthias Scheffler for helpful discussions. Sh. K. S. gratefully acknowledges the Max-Planck-Gesellschaft for financial support.

*Permanent address: Boreskov Institute of Catalysis, Novosibirsk, 630090 Russia.
†Author to whom correspondence should be addressed. FAX: (+49 30) 8413 4401. Electronic address: weiss_w@fhi-berlin.mpg.de

[1] *Adsorption on Ordered Surfaces of Ionic Solids and Thin Films*, edited by H.-J. Freund and E. Umbach, Springer Series in Surface Science Vol. 33 (Springer, Berlin, 1993).
[2] Sh. K. Shaikhudtinov, Y. Joseph, C. Kuhrs, W. Ranke, and W. Weiss, Faraday Discuss. **114** (1999).
[3] V. E. Henrich and P. A. Cox, *The Surface Science of Metal Oxides* (Cambridge University Press, Cambridge, 1994).
[4] Sh. K. Shaikhudtinov and W. Weiss, Surf. Sci. Lett. **432**, L627 (1999).
[5] X.-G. Wang, W. Weiss, Sh. K. Shaikhutdinov, M. Ritter, M. Petersen, F. Wagner, R. Schlögl, and M. Scheffler, Phys. Rev. Lett. **81**, 1038 (1998).
[6] W. Weiss, D. Zscherpel, and R. Schlögl, Catal. Lett. **52**, 215 (1998).
[7] A. R. Lennie, N. G. Condon, F. M. Leibsle, P. W. Murray, G. Thornton, and D. J. Vaughan, Phys. Rev. B **53**, 10 244 (1996).
[8] N. G. Condon, F. M. Leibsle, T. Parker, A. R. Lennie, D. J. Vaughan, and G. Thornton, Phys. Rev. B **55**, 15 885 (1997).
[9] N. G. Condon, F. M. Leibsle, A. R. Lennie, P. W. Murray, D. J. Vaughan, and G. Thornton, Phys. Rev. Lett. **75**, 1961 (1995).
[10] M. Ritter and W. Weiss, Surf. Sci. **432**, 81 (1999).
[11] W. Weiss, M. Ritter, D. Zscherpel, M. Swoboda, and R. Schlögl, J. Vac. Sci. Technol. A **16**, 21 (1998).
[12] W. Weiss and M. Ritter, Phys. Rev. B **59**, 5201 (1999).
[13] R. W. G. Wyckoff, *Crystal Structures*, 2nd ed. (Interscience, New York, 1982), Vol. I, p. 85.
[14] C. Noguera, *Physics and Chemistry at Oxide Surfaces* (Cambridge University Press, Cambridge, 1996)
[15] J. Goniakowski and C. Noguera, Surf. Sci. **319**, 68 (1994).
[16] M. Tsukada, E. Miyazaki, and H. Adachi, J. Phys. Soc. Jpn. **50**, 3932 (1981).
[17] H. Over, U. Ketterl, W. Mortiz, and G. Ertl, Phys. Rev. B **46**, 15 438 (1992).
[18] A. Muan, Am. J. Sci. **256**, 171 (1958).